

Broadband, Dead-Time-Free Spectrometer Using RFSoc for WISP Dark Matter Searches

Hiroki Takeuchi¹, Junya Suzuki¹, Shunsuke Adachi^{2, 1}, and Osamu Tajima¹

¹*Department of Physics, Faculty of Science, Kyoto University, Kyoto 606-8502, Japan*

**E-mail: takeuchi.hiroki.74w@st.kyoto-u.ac.jp*

²*Hakubi Center for Advanced Research, Kyoto University, Kyoto 606-8501, Japan*

.....
 Ultra-light dark matter candidates, such as axions and dark photons, particularly within the mass range of μeV to meV , have garnered significant research interest. However, the effectiveness of existing experiments is often hindered by the narrow bandwidths of conventional spectrometers. This study presents a novel spectrometer solution based on a RFSoc, which integrates a high-speed data converter, field programmable gate array (FPGA), and a CPU within a single chip. The spectrometer's programmable logic implements an optimized fast Fourier transform (FFT) that minimizes memory usage, enabling an instantaneous bandwidth of 4 GHz with a frequency resolution of 16 kHz. This configuration achieves more than 99.6% time efficiency, effectively doubling search efficiency, compared with traditional approaches. This paper provides a comprehensive description of the hardware architecture, FPGA firmware, and software implementation, with a focus on the resource-efficient pipelined FFT algorithm. Performance validation results are also presented, demonstrating the accuracy and time efficiency of the developed spectrometer, highlighting its potential for advancing dark matter search.

.....
 Subject Index xxx, xxx

1 Introduction

Dark matter constitutes 26.8% of the total energy density of the universe [1], yet its nature remains elusive. Understanding dark matter is a crucial issue in both cosmology and particle physics. Owing to the limited knowledge about the properties of dark matter, researchers are exploring a wide range of potential candidates with varying mass scales for the particle. In recent years, a group of particles, known as weakly interacting slim particles has attracted attention as a dark matter candidate [2], including axions and dark photons.

Axions and dark photons can be converted into ordinary photons, allowing for experiments aimed at detecting dark matter candidates. The dish-antenna method proposed in Ref. [3] enables the exploration of a broad range of particle masses. The experimental setup involves a mirror (with a magnet for axion searches), receiver circuit, and spectrometer. The frequency distribution of the conversion photon displays a sharp peak at $\nu_0 = m_{\text{DM}}c^2/h$ with a full width at half maximum of $\Delta\nu/\nu_0 \sim 10^{-6}$ when assuming the isothermal halo model for the velocity distribution of dark matter. Here, m_{DM} represents the mass of a particle, and c represents the speed of light. h denotes the Planck's constant. Therefore, the detection of axions or dark photons can be achieved by observing the signal spectrum received by a spectrometer and identifying this spectral peak. The dark photon and axion are characterized by two main parameters: their mass and coupling constant with photons, denoted as χ and $g_{a\gamma\gamma}$ for the dark photon and axion, respectively. When a spectral peak is detected, the mass m_{DM} can be determined by the peak frequency, whereas the coupling constant χ or $g_{a\gamma\gamma}$ can be determined by the intensity of the conversion photon. Past studies [4–9] utilizing the dish-antenna method have achieved direct searches with a sensitivity that surpasses the indirect constraints of cosmology [2, 10].

Among these studies, Refs. [6, 7] did not fully utilize the wide-band nature of the dish-antenna method, owing to the limited bandwidth of the spectrometers employed. They instead employed commercial signal analyzers, which restricted their study to a narrow bandwidth of 2 MHz. Conversely, an antenna and radio-frequency (RF) circuit can cover a wide frequency range of $O(\text{GHz})$, allowing for simultaneous searches across the full spectrum. For these experiments, a spectrometer capable of analyzing over 1 GHz bandwidth simultaneously is needed. Notable attempts to develop such a wide-band spectrometer include Fourier transform versions that require graphical processing units (GPUs) or field-programmable gate arrays (FPGAs). For example, in Ref. [8], a GPU was used to analyze a 4 GHz band with a time efficiency of 60%. Notably, commercial FPGA-based spectrometers can provide dead-time-free analyses over a 2.5 GHz bandwidth [11].

This study presents a dead-time free spectrometer with 4 GHz bandwidth. The spectrometer is built on an RFSoc 2x2 board, utilizing an RFSoc chip that integrates high-speed data converters, FPGA, and CPU [12]. The performance evaluation of this spectrometer is also discussed in detail.

2 Design Strategy and Implementation Method

2.1 Requirements

One key specification that directly impacts search efficiency is called the “instantaneous bandwidth,” which refers to the frequency bandwidth around the center frequency that can be acquired in a single measurement. The upper limit of the instantaneous bandwidth is determined by the sampling rate of the analog-to-digital converter (ADC), responsible for converting analog signals to digital signals. Given the bandwidth capabilities of current high-speed ADCs, our goal was to achieve a bandwidth in the range of several GHz.

Moreover, efficient signal processing is essential to maximize time efficiency and must be performed with no dead time.

Additionally, achieving a high-frequency resolution is crucial for identifying spectral peaks. To search for signals around 30 GHz, a frequency resolution of 30 kHz is required. This specific frequency range has not been explored in previous studies on axion or dark photon searches. With an instantaneous bandwidth of 4 GHz, dividing the band into 1.3×10^5 points is necessary to achieve the desired resolution.

2.2 Hardware Design

To satisfy the above requirements, a high-speed ADC capable of several giga-samples per second (GSPS) is needed, along with a high-performance FPGA capable of processing the ADC output. For this, we employed an AMD Xilinx chip known as the RFSoc [12], which integrates a CPU, FPGA, ADCs, DACs, and other RF circuits into a single system on chip (SoC). Additionally, the processing system (PS) housing the CPU and the programmable logic (PL) housing the FPGA were both connected to external dynamic random access memory (DRAM) chips.

An overview of the spectrometer design and a photograph of the developed spectrometer setup is shown in Fig. 1. Detailed descriptions of each block will be provided in the following sections. The spectrometer components were selected to target a frequency of approximately 30 GHz, and a Marki microwave MMIQ-1040LS was utilized as the IQ mixer. Notably, with different IQ mixer models, the spectrometer can be utilized for a variety of frequency bands. A HiTech Global RFSoc 2x2 board [13] equipped with the ZYNQ UltraScale+ RFSoc

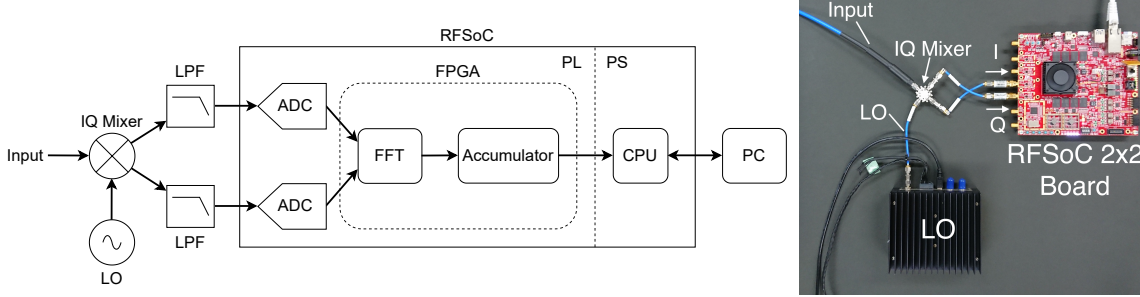


Fig. 1: (Left) Schematic of RF circuits and digital signal processing. The input signal is down-converted by utilizing the IQ mixer and sent to the RFSoc. There, the down-converted signals are converted to digital time-series signals by the 4 GSPS ADCs, and the power spectrum is obtained using the parallel FFT circuit on the FPGA. An accumulator circuit calculates the time average, with the obtained power spectrum transferred to the embedded CPU, which is then sent to an external computer over Ethernet. (Right) Photo of our proposed spectrometer.

XCZU28DR, was used, featuring two 12-bit 4.096 GSPS ADCs, and a 1 Gbps Ethernet cable was used for external communications. ADC synchronization was achieved using the reference clock on the RFSoc board. The IQ mixer and ADCs are connected through SMA cables, with a low-pass filter (Mini-Circuits VLFG-1800+) inserted between them to limit the signal to below 2 GHz.

To detect spectral peaks with a width of approximately 10^{-6} times 30 GHz, we set the FFT size to $N = 2^{17}$ to achieve a frequency resolution of 31.25 kHz¹. Subsequently, we developed a high-resolution version with an FFT size of $N = 2^{18}$, providing a frequency resolution of 15.625 kHz.

The data acquired by the ADCs were streamed to the PL through the RF data converter’s intellectual property (IP) core, whose output was 512 MHz with eight time points per clock cycle (Fig. 2).

2.3 Firmware Design

2.3.1 Clock Frequency Conversion and FFT

Operating signal processing at 512 MHz presents challenges in satisfying PL-resource timing constraints. To address this issue, we utilized input distribution and asynchronous

¹ 4.096 GHz bandwidth / $2^{17} = 31.25$ kHz

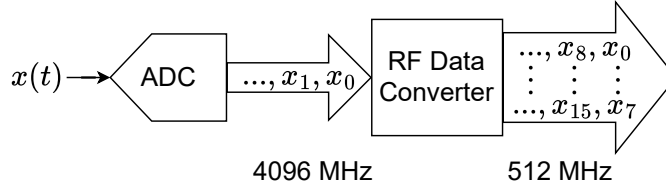


Fig. 2: Signal handling by the RF data converter. The ADC receives data at 4.096 GSPS and transmits it to the RF data converter on the FPGA. The RF data converter operates at 512 MHz, which corresponds to 1/8 of the ADC clock frequency, and outputs data from eight time points per clock cycle.

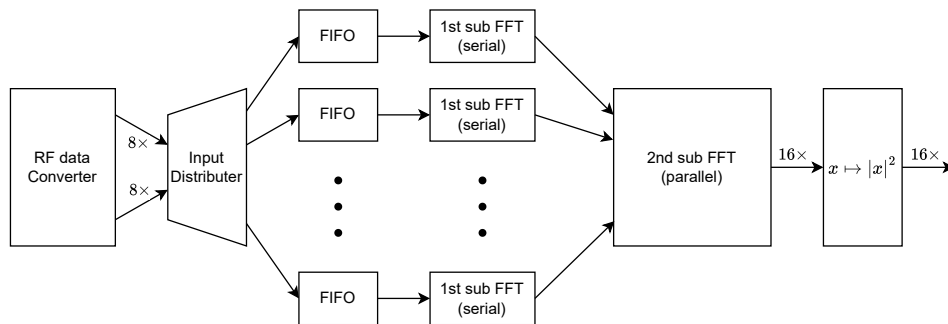


Fig. 3: Block diagram of the FFT block. Signal processing is performed by four types of IPs from left to right: input distribution circuit (asynchronous FIFO), first sub-FFT circuit (serial FFT), second sub-FFT (parallel FFT), and power spectrum calculation circuit.

first-in-first-out (FIFO) logic to increase the number of data lanes to 16 while reducing the clock frequency by half.

Subsequently, ADC signals were converted into a power spectrum using an FFT block. Further details regarding the FFT circuit can be found in Section 3. Following the FFT computation, the power spectrum was determined from the resulting complex spectrum. The block diagram is shown in Fig. 3. The input distribution circuit, secondary sub-FFT circuits, and power spectrum calculation circuits were implemented through high-level synthesis (HLS), which involves converting C++ code into a hardware description language. A Vitis HLS was used, and existing IPs were integrated for clock conversions and initial sub-FFT computations.

To align the output to the accumulator circuit, it was configured as a 54 bit fixed-point number for the $N = 2^{17}$ FFT circuit specification or a 32 bit floating-point number for the $N = 2^{18}$ FFT circuit specification. These specifications are listed in Table 1.

Table 1: Specifications of the FFT block.

Specification	$N = 2^{17}$	$N = 2^{18}$
Parallel channels	16	16
Input format	Fixed-point	Fixed-point
Input bit width	12 bits	12 bits
Format at FFT completion	Fixed-point	Fixed-point
Bit width at FFT completion	29 bits	30 bits
Output format	Fixed-point	Floating-point
Output bit width	54 bits	32 bits

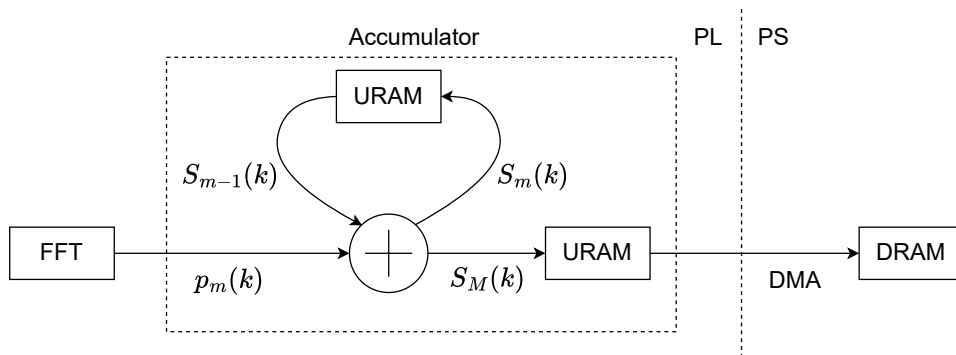


Fig. 4: Overview of the accumulator circuit. The time average of the power spectrum output from the FFT circuit was calculated on the FPGA and transferred to the DRAM in the PS through DMA for processing by the CPU.

2.3.2 Accumulator Block

An accumulator circuit calculates the time average (sum) of the power spectrum, effectively reducing the data rate before transferring it to the PS. An overview of the accumulator circuit is shown in Fig. 4. Initially, the power spectrum was fed from the FFT circuit, with the partial sum temporarily stored in the UltraRAM (URAM) on the PL. After accumulating data from M iterations, the final result was then transferred to a data buffer, constructed using the URAM resource. This entire process was performed simultaneously for 16 values at a frequency index ok .

For a set averaging count of $M = 1024$ and an $N = 2^{17}$ FFT circuit, the input width is 54 bit, and the output width is 64 bit. However, for an FFT circuit with $N = 2^{18}$, both input and output utilize 32 bit floating-point numbers (Table 2). Notably, the accumulator circuit was implemented entirely through high-level synthesis.

Table 2: Specifications of the accumulator circuit.

Specification	$N = 2^{17}$	$N = 2^{18}$
Averaging count M	1024	1024
Input format	Fixed-point	Floating-point
Input bit width	54 bit	32 bit
Output format	Fixed-point	Floating-point
Output bit width	64 bit	32 bit

Table 3: FPGA resource utilization of the spectrometer

Resource Type	Utilization		Usage		Available
	$N = 2^{17}$	$N = 2^{18}$	$N = 2^{17}$	$N = 2^{18}$	
LUT	20.0%	25.5%	85 k	108 k	425 k
FF	18.5%	20.7%	157 k	176 k	851 k
BRAM	14.5%	24.8%	157	268	1080
URAM	77.5%	80.0%	62	64	80
DSP	15.8%	15.9%	674	678	4272

2.3.3 Resource Usage

The total amount of resources in the FPGA of the RFSoc and the amount of resources utilized are listed in Table 3. Apart from the URAM, which stores FFT results in the accumulation block, each resource type was utilized at less than 50%, which allows for expansion through parallelization, as well as increasing the FFT size. URAM was primarily allocated for storing FFT results in the accumulation block, and its resource consumption could be minimized by decreasing the arithmetic precision of the stored data. We successfully implemented firmware with FFT circuits with $N = 2^{17}$ at 64 bit fixed-point numbers and $N = 2^{18}$, with precision limited to 32 bit floating-point numbers. Our spectrometer specifications are listed in Table 4.

The FFT circuit achieved a throughput surpassing the ADC sampling rate, enabling the full 4.096 GHz bandwidth of the ADC to be utilized. Additionally, a resolution of 15.6 kHz was achieved, which is suitable for the target signal at approximately 30 GHz.

Table 4: Summary of specifications of the developed spectrometer

Item	Performance Value
Frequency Bandwidth	4.096 GHz
Input	Complex (IQ)
FFT Size	$2^{17} / 2^{18}$
Frequency Resolution	31.25 kHz / 15.625 kHz
ADC Resolution	12 bit
ADC Sampling Rate	4.096 GSPS
FFT Circuit Throughput	4.800 GSPS
Time Averaging Interval	32.768 ms / 65.536 ms

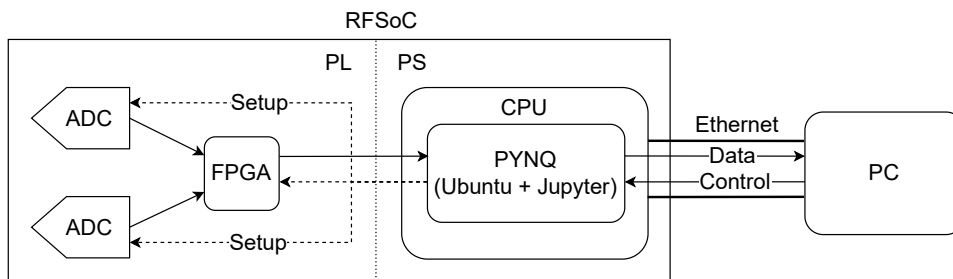


Fig. 5: Overview of the software component. Python scripts were run on PYNQ to perform the initial setup of the FPGA and ADCs, clock synchronization settings for the two ADCs, and transfer of the spectrum obtained by the FPGA to the PC.

2.4 Software Design

An overview of the interface between the firmware and software is shown in Fig. 5. Data were reordered from bit-reverse to natural order after accumulation on the PL and subsequently transferred to the PS’s DRAM through an Advanced eXtensible Interface (AXI) port utilizing Xilinx’s direct memory access (DMA) core. To facilitate physical routing during implementation, the DMA circuit operated at 100 MHz.

Subsequently, the data were time-averaged in the PS and transmitted to an external PC through a gigabit Ethernet cable on the PS side using the ZeroMQ library [14]. The PYNQ framework [15] was employed for PL reconfiguration, data transmission, and post-processing.

On the external PC, a standard Python script was utilized to communicate with the RFSoc and to store the received data.

3 Resource-Efficient Implementation of the FFT Circuit on FPGA

This section describes our resource-efficient implementation methods for pipelined FFT circuits. These methods were utilized in the design of our spectrometer to minimize circuit area, ensuring compatibility with the limited resources available in the PL of the RFSoc chip. In the implementation of the FFT circuit, the rotation circuit must be efficient, as it demands significant circuit resources and consumes a substantial amount of memory (e.g., for complex multiplication with several coefficients). To reduce memory consumption, we divided the rotation process into two stages and employed a Radix-2⁴ architecture [16, 17].

3.1 Basics of the Pipelined FFT and the Terminology

In an FFT-based spectrometer, the time-series input data, $x(t)$, are converted into a frequency spectrum, $\tilde{x}(k)$, through a discrete Fourier transform (DFT):

$$\tilde{x}(k) = \sum_{t=0}^{N-1} W_N^{kt} x(t), \quad (1)$$

where N represents the length of the DFT, and k, t assume integer values from 0 to $N - 1$. W_N is defined as $W_N = e^{-2\pi i \frac{1}{N}}$, representing the N th primitive root of unity. The Cooley-Tukey algorithm [18], generally referred to as the FFT, reduces the computational cost of DFT from $O(N^2)$ to $O(N \log N)$ by recursively breaking down the DFT into smaller components. For $N = 2^n$, $\tilde{x}(k)$ is described as follows:

$$\begin{aligned} \tilde{x}(k) = & \sum_{t_0=0}^1 W_2^{k_{n-1}t_0} W_{2^n}^{k_{0:n-2}t_0} \sum_{t_1=0}^1 W_2^{k_{n-2}t_1} W_{2^{n-1}}^{k_{0:n-3}t_1} \\ & \dots \sum_{t_{n-2}=0}^1 W_2^{k_1t_{n-2}} W_{2^2}^{k_0t_{n-2}} \sum_{t_{n-1}=0}^1 W_2^{k_0t_{n-1}} x(t). \end{aligned} \quad (2)$$

Here, for a non-negative integer x represented in binary notation, x_i denotes its i th digit from the right, whereas $x_{i:j}$ represents the number from the i th to j th digits. For example, if $x = 6$ (binary: $110^{(2)}$), then $x_0 = 0, x_{1:2} = 3$.

The concept of pipelined FFT, which implements FFT as a continuous pipelined flow in a circuit, was proposed [19, 20] and has been widely utilized in achieving high throughput. Various circuit architectures have been proposed to cater to a wide range of applications [21].

The schematic of the single-path delay feedback (SDF) architecture of the pipelined FFT is shown in Fig. 6, whereas the multi-path delay feedback (MDF) architecture, which can achieve twice or even higher throughput, is shown in Fig. 7. By examining the twiddle

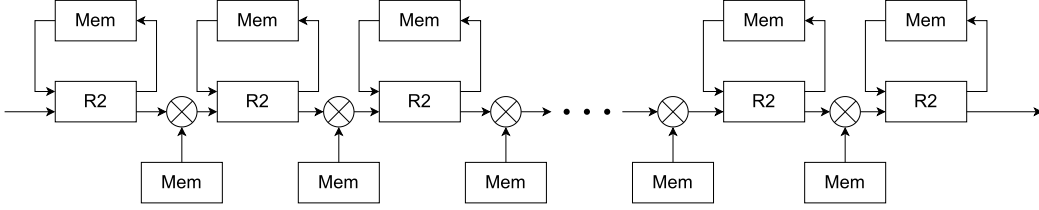


Fig. 6: Structure of the SDF pipeline circuit. “R2” denotes a Radix-2 butterfly operation, and “Mem” represents a memory for temporary data storage or a table for rotation operation.

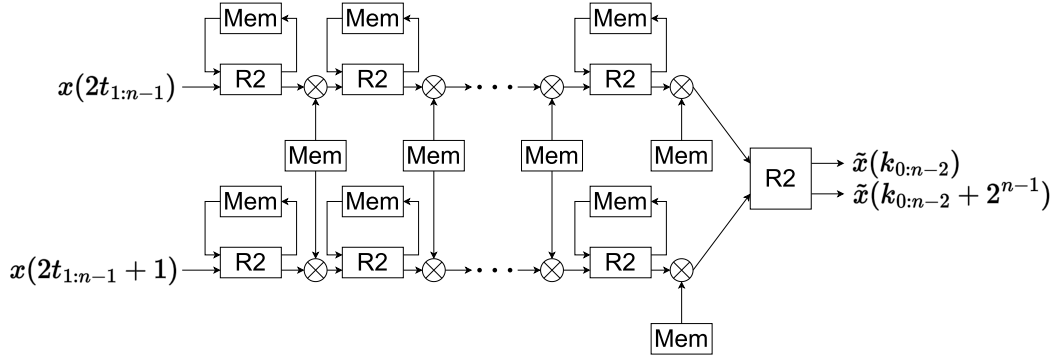


Fig. 7: Two-parallel MDF architecture comprising two SDF circuits and a Radix-2 butterfly unit, achieving doubled throughput.

factors $W_2 (= -1)$ and W_{2^k} in Eq. (2), the FFT can be expressed as a combination of 2-point FFT, which transforms input A and B into $A + B$ and $A - B$, along with a general rotation by the power of W_{2^k} . The former process is known as a (Radix-2) butterfly operation (“R2” in the figures). The latter is typically implemented using a look-up table (LUT), where pre-computed twiddle factors are stored and retrieved for multiplication at runtime. Although this approach requires $O(2^k)$ memory size for computing powers of W_{2^k} , it can be implemented using a single complex multiplier. In the SDF architecture, which processes one input per clock cycle, temporary memory is utilized to store input data so that the butterfly operation can be executed using subsequent inputs. The 2-parallel MDF architecture shown in Fig. 7 features two SDF circuits in parallel, each handling even- and odd-indexed data input. These circuits merge their outputs at the end to produce the upper and lower halves of the frequency domain data simultaneously.

3.2 Resource Reduction Techniques for Pipelined FFT

3.2.1 Memory Reduction of the Rotation Unit by Splitting the Twiddle Factor Table

The memory requirements for the rotation process, shown in Eq. (2) and Fig. 6, are directly proportional to the FFT length. For an FFT length of $N = 2^n$ ($n = 17$ or 18), approximately 10 Mbit of memory is required to implement a rotation. To facilitate simultaneous access to the twiddle factor table at each stage, distributed memory resources, such as block RAM (BRAM) on FPGA are used to enable high-bandwidth random access. Given the limited availability of BRAM resources, we optimized memory utilization for the rotation unit by partitioning the twiddle factor table.

First, the size of the twiddle factor table was reduced by factoring W_4 from general W_N :

$$W_N^m = W_4^{m_{n-2:n-1}} W_N^{m_{0:n-3}},$$

because multiplication of $W_4 = i$ or its power can be easily performed using a sign flip and swapping real and imaginary components.

To further minimize memory utilization, we set $L = 2^l (< N)$ and decomposed it into a product of three twiddle factors:

$$W_N^m = W_4^{m_{n-2:n-1}} W_{\frac{N}{L}}^{m_{l:n-3}} W_N^{m_{0:l-1}}, \quad (3)$$

where $W_{\frac{N}{L}}^{m_{l:n-3}}$ represents a coarse rotation and $W_N^{m_{0:l-1}}$ represents a fine rotation. Because $m_{0:l-1}$ is an integer in the range $[0, L)$, $2L$ real numbers are required to store $W_N^{m_{0:l-1}}$. Similarly, because $m_{l:n-3}$ is an integer in the range $[0, \frac{N}{4L})$, $2 \times \frac{N}{4L}$ real numbers are sufficient for storing $W_{\frac{N}{L}}^{m_{l:n-3}}$. Moreover, by leveraging the symmetry inherent in cosine and sine functions, the memory requirement for $W_{\frac{N}{L}}^{m_{l:n-3}}$ can be reduced to $\frac{N}{4L}$ real numbers. Hence, through the computation of Eq. (3) using the circuit depicted in Fig. 8, the rotation operation can be executed utilizing a total memory of only $2L + \frac{N}{4L}$ real numbers. This rotation unit configuration is henceforth referred to as a “split LUT rotation unit.”

The memory usage of the split LUT rotation unit is minimized when, for $N = 2^n$, $L = 2^{\frac{n-3}{2}}$ if n is odd, or $L = 2^{\frac{n-4}{2}}, 2^{\frac{n-2}{2}}$ if n is even. This memory requires $\sqrt{2N}$ real numbers for odd n , and $\frac{3}{2}\sqrt{N}$ real numbers for even n . Because the required memory for a conventional rotation unit is $N/4$ real numbers, our memory usage is reduced by an order of magnitude. For example, $N = 2^{17}$ can be reduced to 1/64. Alternatively, the number of required arithmetic units (e.g., multipliers) is approximately doubled because the rotation operation must be performed twice. To address this tradeoff, we used the split LUT rotation only for the rotation units requiring the largest LUT size. These units require sixteen times more LUT size than the second largest ones.

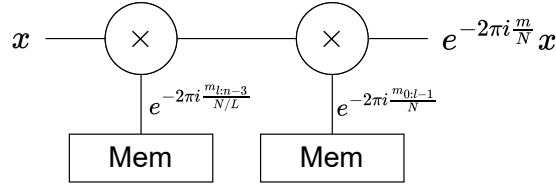


Fig. 8: Overview of the developed split LUT rotation unit. By splitting the rotation into two components, the number of complex multiplications doubled compared with those of the conventional LUT rotation unit; however, the rotation memory utilization was significantly reduced from $O(N)$ to $O(\sqrt{N})$.

3.2.2 Radix-2⁴ MDF Architecture

As demonstrated, LUT splitting reduces the memory consumption in the general rotation units. Furthermore, the number of general rotation units can be reduced by optimizing the architecture. Hence, we adopted the Radix-2⁴ MDF architecture [16, 17], characterized by the fewest general rotation units for a 16-parallel FFT circuit.

We split k and t as $k = k_{0:n-5} + 2^{n-4}k_{n-4:n-1}$, $t = t_{0:3} + 2^4t_{4:n-1}$ and computed the results as follows:

$$\tilde{x}(k) = \sum_{t_{0:3}=0}^{15} \sum_{t_{4:n-1}=0}^{2^{n-4}-1} W_N^{(k_{0:n-5}+2^{n-4}k_{n-4:n-1})(t_{0:3}+2^4t_{4:n-1})} x(t) \quad (4)$$

$$= \sum_{t_{0:3}=0}^{15} W_{2^4}^{k_{n-4:n-1}t_{0:3}} W_N^{k_{0:n-5}t_{0:3}} \sum_{t_{4:n-1}=0}^{2^{n-4}-1} W_{2^{n-4}}^{k_{0:n-5}t_{4:n-1}} x(t). \quad (5)$$

The inner sum comprises isolated DFTs of size $\frac{N}{16}$ and the outer sum involves a combination of rotation operations and a size-16 DFT, processed using 15 rotation units and a fully parallelized 16-parallel FFT circuit. Within this circuit, we split $k_{n-4:n-1}$ and $t_{0:3}$, and computed the results as follows:

$$\begin{aligned} \sum_{t_{0:3}=0}^{15} W_{2^4}^{k_{n-4:n-1}t_{0:3}} &= \sum_{t_0=0}^1 W_2^{k_{n-1}t_0} W_4^{k_{n-2}t_0} \sum_{t_1=0}^1 W_2^{k_{n-2}t_1} W_{16}^{k_{n-4:n-3}t_{0:1}} \\ &\quad \sum_{t_2=0}^1 W_2^{k_{n-3}t_2} W_4^{k_{n-4}t_2} \sum_{t_3=0}^1 W_2^{k_{n-4}t_3}. \end{aligned} \quad (6)$$

Among the rotation operations performed in Eq. (6), the components represented by W_2^m and W_4^m can be expressed through sign inversion, including swapping the real and imaginary parts, which eliminates the need for multipliers. Moreover, as the values of $k_{n-4:n-3}$ and $t_{0:1}$

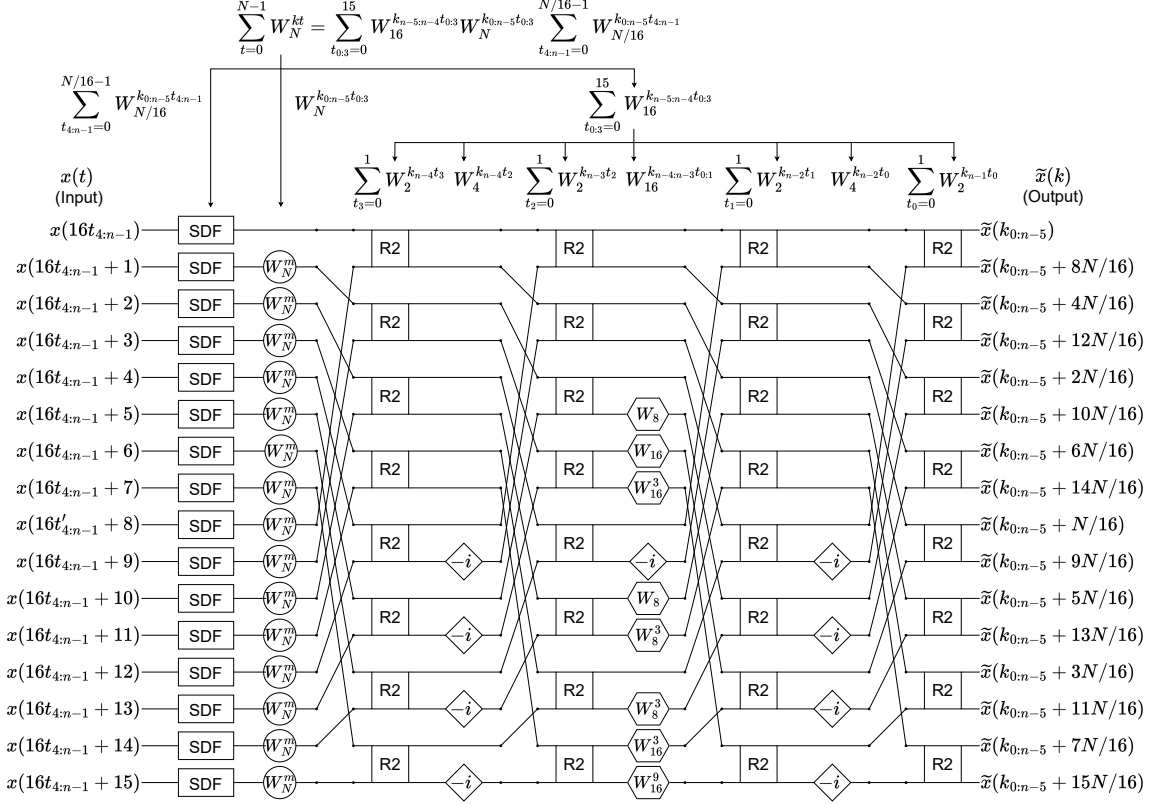


Fig. 9: FFT circuit configuration. The calculation was divided into 16 SDF circuits and a 16-parallel MDF FFT circuit. The latter was further divided into a Radix- 2^4 circuit based on Eq. (6), comprising Radix-2 butterfly units (R2), $-i$ multipliers (diamond), constant rotation units (hexagon), and general rotation units (circle). The general rotation units employ the split LUT method to reduce memory utilization.

are predetermined, the rotation operation $W_{16}^{k_{n-4;n-3}t_{0:1}}$ can be executed using a constant multiplier. Although W_{16} cannot reduce the number of multiplications, unlike W_2 or W_4 , the cost of constant multiplication is minimal, and no rotation memory is required as the rotation angle is known.

The configuration shown in Fig. 9 can be obtained by constructing the circuit from Eqs. (5) and (6). We adopted Xilinx's FFT core for the 16 SDF circuits and a split LUT rotation unit for general rotation following each circuit. The Radix- 2^4 architecture reduced the number of general rotation units to 15. For comparison, the original Radix-2 architecture utilized 32 units, whereas the Radix- 2^2 architecture, which is widely utilized, requires 24 units.

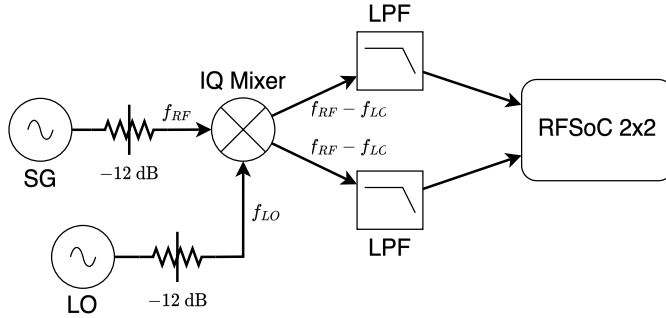


Fig. 10: Test setup for spectroscopy and linearity measurement. The input signal (RF) (16 GHz) and LO signal (15 GHz) were generated using signal generators, and attenuated by 12 dB.

4 Performance Evaluation

We evaluated the performance and linearity of our spectroscopy method using a monotone RF source as input to the spectrometer. Additionally, we assessed the time efficiency of the spectrometer using a blackbody radiation source.

We conducted a basic operational check by observing a monotone RF signal with the developed spectrometer. Input and LO signals were generated using a signal generator (NATIONAL INSTRUMENTS FSL-0020), as shown in Fig. 10. The input signal was set to 16 GHz, whereas the LO frequency was set to 15 GHz, resulting in an intermediate frequency (IF) signal of 1 GHz input to the RFSoc.

4.1 Demonstration of Spectrometry Operation Using a Monotone RF Source

The observed spectrum is shown in Fig. 11a, where the peak was accurately observed in the 16 GHz bin. The leakage from the IQ mixer imbalance and harmonics were all at least 20 dB compared with the signal, aligning with the catalog values of the IQ mixer. The noise floor was approximately $\sim 150 \text{ dB}_{\text{fs}}/\text{Hz}$, also consistent with ADC catalog specifications, thus validating the absence of additional noise in the FFT circuit on the FPGA.

In Fig. 11b, an enlarged view of the 16 GHz signal reveals symmetric sidelobes around the center, attributable to the DFT calculated within a finite interval and several data points. This observation aligns with expectations when utilizing a rectangular window (i.e., no window function).

The spectrum exhibits spurious peaks originating from the following sources:

- (i) Components originating from $1/f$ noise near DC (0 MHz and 2048 MHz)
- (ii) Leakage of (i) into parallel-computed components (512 MHz, 1024 MHz, 1536 MHz, ...)

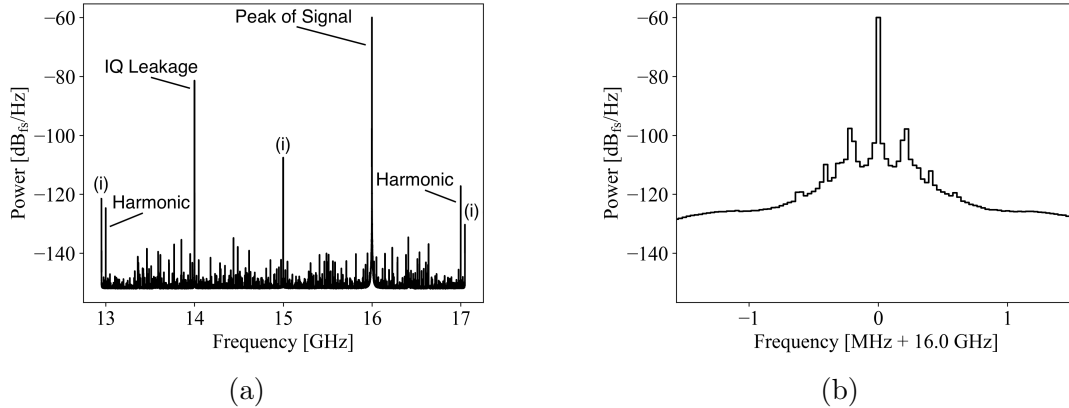


Fig. 11: Power spectrum when a 16 GHz signal was input. (a) Complete power spectrum. The peak was accurately observed at 16 GHz, with all other peaks being at least 20 dB lower. The noise floor was approximately ~ -150 dB_{fs}/Hz. (b) Power spectrum near the peak. The peak was accurately located at 16 GHz, and the leakage was at least 30 dB lower.

(iii) Clock frequency 40.96 MHz and its harmonics

The spurious results from (i) are shown in Fig. 11a. To mitigate the impact of these spurious peaks, dark matter search experiments should be conducted using multiple LO frequencies.

For the evaluations conducted, a total bandwidth of 50 MHz was excluded: 10 MHz width for each (i), 1 MHz width for each (ii), and 0.25 MHz width for each (iii).

4.2 Linearity

Subsequently, the linearity of the spectrometer response was assessed. A monotone signal at 14 GHz was generated using a signal generator (KEYSIGHT E8257D) at 0.05–2.00 mW, which was then attenuated by -60 dB. This power level was adjusted to match that of the previous experiment [6], and the LO frequency was set to 13 GHz.

The relationship between the input and observed power values is shown in Fig. 12. The obtained power values were fitted to a linear function with an offset and the residuals were calculated from the linear line. We validated the linearity with an accuracy within 0.5%. The coupling constant, χ or $g_{a\gamma}$, is directly proportional to the square root of the observed power. Consequently, the impact of the non-linearity on the coupling constant is less than 0.25%.

4.3 Stability and Time Efficiency

To assess the stability of the developed system, we conducted a 24-h continuous operation test. Data were set to be transmitted from the FPGA every 65.536 ms, and the system was

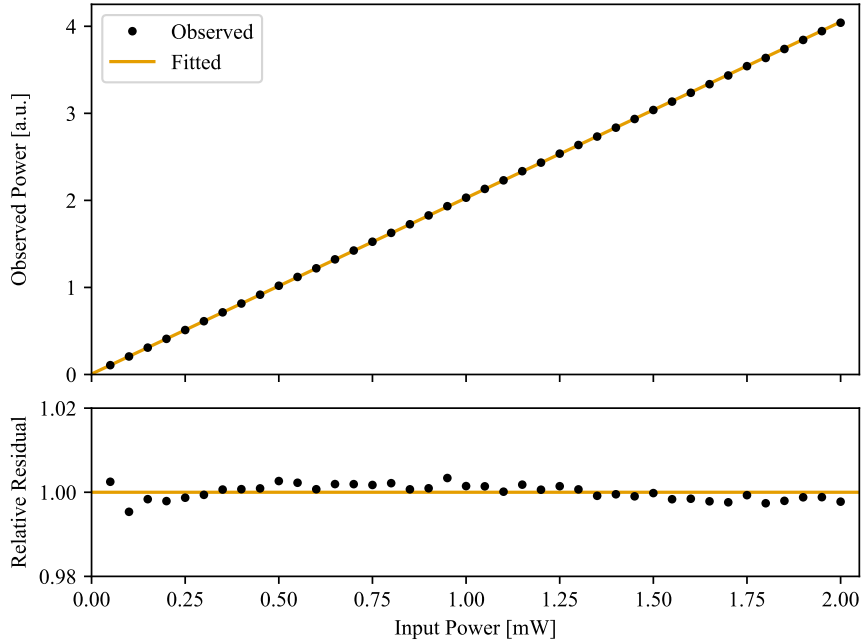


Fig. 12: Relationship between input and observed power. The linearity was validated with an accuracy within 0.5%.

configured to receive data continuously for 1,318,360 cycles, equivalent to precisely 24 h. The total time required was 24 h, 44 s, demonstrating that data acquisition was successful more than 99.94% of the time.

Furthermore, we conducted tests to ensure that each 65.536 ms measurement interval was executed with no inefficiencies. This was achieved by analyzing the power fluctuations. The power P and power fluctuation ΔP observed when measuring blackbody radiation with a radio-wave receiver connected to the developed spectrometer in the Rayleigh-Jeans regime can be as follows [22]:

$$P = Gk_B T_{\text{sys}} \Delta\nu, \quad (7)$$

$$\Delta P = \frac{Gk_B T_{\text{sys}} \Delta\nu}{\sqrt{\epsilon \Delta t \Delta\nu}}, \quad (8)$$

where G denotes the system gain, T_{sys} represents the system temperature primarily determined from the blackbody temperature and thermal noise from the amplifier, $\Delta\nu$ represents the width of the observed frequency band, Δt represents the measurement time, and ϵ represents the time efficiency of the observation. This property enables the calculation of ϵ as follows:

$$\epsilon = \frac{1}{\Delta\nu \Delta t} \left(\frac{P}{\Delta P} \right)^2. \quad (9)$$

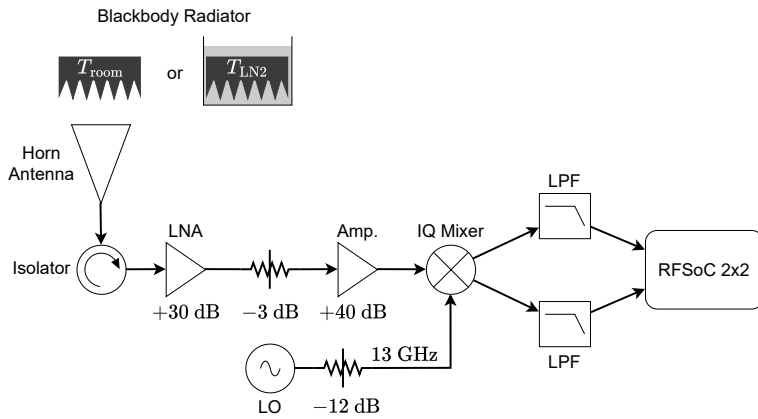


Fig. 13: Setup for measuring time efficiency. The radiation from the blackbody was received by the horn antenna. The signal was amplified using two amplifiers, downconverted by an IQ mixer with an LO frequency of 13 GHz, and then spectrometered on the RFSoc 2x2 board ranging from 11–15 GHz. Power spectra were measured for the blackbody at room temperature and the blackbody at 77 K immersed in liquid nitrogen.

The measurement setup is shown in Fig. 13. We received radiation from a blackbody radiator at room temperature (13°C) or at 77 K, achieved by immersing it in liquid nitrogen. The power spectra were then measured using our spectrometer. The CV-3 model from E&C Engineering was utilized for the blackbody radiator, whereas the PE9856/SF-20 model from PASTERNAK was utilized for the horn antenna. An isolator (PASTERNAK PE8304) was inserted between the horn antenna and the first amplifier (low noise factory LNF-LNR6_20A), followed by the second amplifier (Mini-Circuits ZVA-18G-S+). An attenuator was inserted between the first and second amplifiers for gain adjustments. The spectrometer was configured with an LO frequency of 13 GHz, and each measurement lasted for 65.5 s, with intervals of 65.5 ms repeated 1000 times at both temperatures. Frequency bands affected by external noise from the folding of the Wi-Fi were excluded from the analysis.

When ΔP was assumed to be Gaussian white noise, $1/\epsilon$ followed a chi-squared distribution from Eq. (9). Instead of directly calculating ϵ , the unbiased $1/\epsilon$ must be calculated first, followed by the computation of ϵ from the outcome (Appendix A). Therefore, for each frequency, we calculated the time average of the power spectrum, fluctuation of the measured values, and subsequently computed $1/\epsilon(\nu)$. Next, $1/\epsilon$ was obtained from the average of these values. The values of $1/\epsilon$ obtained for each frequency and its histogram are shown in Fig. 14. From the measurement of room-temperature blackbody radiation, we obtained $1/\epsilon = 1.00257(13)$, and from the measurement of the 77 K blackbody, we obtained

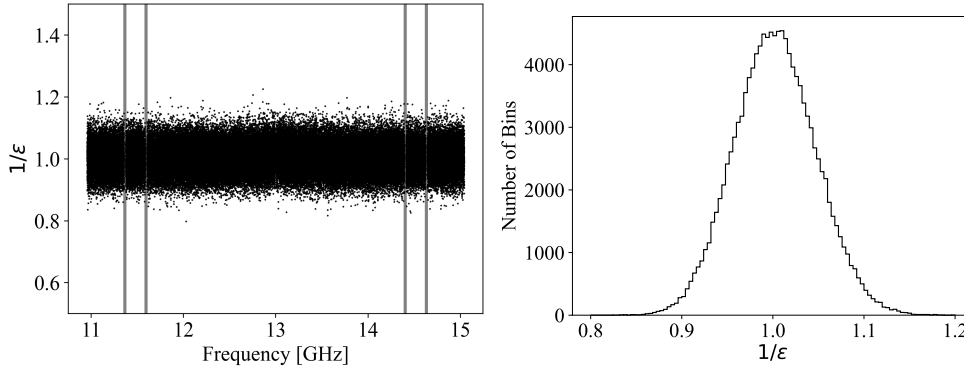


Fig. 14: (Left) Measured values of $1/\epsilon$ at each frequency for room-temperature blackbody radiation. The frequency bands impacted by the folding noise of the Wi-Fi (represented by the thick gray lines) were excluded. (Right) Histogram of the measured $1/\epsilon$. The distribution was closely centered around unity, indicating a spectrometer efficiency of approximately 100%. Similar outcomes were observed during the blackbody measurement at 77 K.

$1/\epsilon = 1.001\,69(13)$. Both measurements ensured that ϵ exceeded 99.7%, thus validating the spectrometer’s capability to perform spectrometry with better than 99.6% time efficiency.

5 Conclusion

This study developed a wide-band spectrometer that enabled spectrometry across a 4 GHz bandwidth, focusing on the need to search for axions and dark photons. Additionally, a frequency resolution of 16 kHz was achieved to detect the extremely narrow spectral peak of the conversion photon, typically $\Delta\nu/\nu \sim 10^{-6}$. With this spectrometer, we anticipate conducting an efficient search and expect an enhancement in the sensitivity of χ or $g_{a\gamma\gamma}$ owing to increased data statistics.

To achieve this performances, we designed the hardware and firmware components, including the logic circuits on the FPGA. To digitize IQ signals, we utilized two ADCs and an IQ mixer, and by incorporating two 4GSPS ADCs within the RFSoc, we secured a bandwidth of 4 GHz. Furthermore, on the built-in FPGA, we implemented FFT conversions through 16-parallel FFT circuits and utilized an accumulator circuit to compress the data, allowing for signal analysis from the ADC with no loss. To minimize the increase in resource consumption of FPGA, resulting from parallelization, we developed a memory-efficient rotation method and implemented a Radix-2⁴ architecture that required fewer general rotation units. These enhancements resulted in the development of a spectrometer with the required performance.

Performance evaluation tests were conducted on the developed spectrometer, which included obtaining the desired spectrum by inputting a monotone RF source and validating linearity at an accuracy within 0.5%. Additionally, we validated the stability of the spectrometer for continuous operation over 24 h and demonstrated its ability to perform spectrometry with greater than 99.6% time efficiency.

The increased statistics provided by this spectrometer will significantly enhance the sensitivity of axion and dark photon searches. Although previous experiments [6, 7] were limited to searching a 2 MHz frequency range at once, our spectrometer allows for a 4 GHz search range, resulting in a time efficiency improvement of over 2000 times. Additionally, our approach achieves approximately twice the search efficiency compared to conventional approaches [8, 11]. Moreover, the developed spectrometer has potential in various fields, including radio astronomy and industry. Furthermore, the current FPGA implementation utilizes fewer than half of the available resources, which allows for potential bandwidth doubling by implementing two FFT circuits and utilizing four ADCs in the next-generation boards Ref. [23].

Acknowledgment

This research was supported by JSPS KAKENHI under grant numbers 22K18713, 23H00111, 24KK0066, and 24KJ1452, as well as support from JST, CREST under grant number JPMJCR23I3. Additionally, this research was supported by grants from the Murata and Sumitomo Foundations. SA acknowledges the Hakubi Project Program of Kyoto University.

A Estimation Method for Time Efficiency ϵ

Section 4.3 delves into time efficiency ϵ , which does not adhere to a normal distribution. Therefore, the precise estimation of ϵ requires care. Hence, this section explains the method of its estimation.

As shown in Section 4.3, the measured value $P_{\text{obs}}(\nu, t)$, of the thermal noise, P , measured within the frequency range ν to $\nu + \Delta\nu$ and time range t to $t + \Delta t$, conforms to a normal distribution with a mean and standard deviation of P and ΔP , respectively. Additionally, P and ΔP are theoretically expected to follow Eqs. (7) and (8).

When $P_{\text{obs}}(\nu, t)$ is measured n_t times with respect to t , $P(\nu)$ can be estimated through the (time) average $\overline{P_{\text{obs}}}(\nu)$ of $P_{\text{obs}}(\nu, t)$, whereas $\Delta P(\nu)^2$ can be estimated using the unbiased variance, $V(P_{\text{obs}})(\nu)$, of $P_{\text{obs}}(\nu, t)$ with respect to t . Given that $P_{\text{obs}}(\nu, t)$ adheres to a normal distribution with variance $P(\nu)^2/(\Delta\nu\epsilon\Delta t)$, $V(P_{\text{obs}})(\nu)^2 \cdot \Delta\nu\epsilon\Delta t/P(\nu)^2$ conforms to a

chi-squared distribution with $n_t - 1$ degrees of freedom. Therefore, defining a random variable, $X_{\text{obs}}(\nu)$, as $X_{\text{obs}}(\nu) = V(P_{\text{obs}}(\nu)^2 \cdot \Delta\nu\Delta t / (P(\nu)^2 \cdot (n_t - 1)))$, the expectation E and the unbiased variance, V , of $X_{\text{obs}}(\nu)$ can be expressed as follows:

$$E(X_{\text{obs}}) = \frac{1}{\epsilon} \quad (\text{A1})$$

$$V(X_{\text{obs}}) = \frac{2}{(n_t - 1)\epsilon^2} \quad (\text{A2})$$

Therefore, $1/\epsilon$ can be estimated from the measurement of X_{obs} .

References

- [1] N. Aghanim et al., *Astron. Astrophys.*, **641**, A6 (September 2020).
- [2] P. Arias, D. Cadamuro, M. Goodsell, J. Jaeckel, J. Redondo, and A. Ringwald, *J. Cosmol. Astropart. P.*, **2012**(06), 013–013 (June 2012).
- [3] D. Horns, J. Jaeckel, A. Lindner, A. Lobanov, J. Redondo, and A. Ringwald, *J. Cosmol. Astropart. P.*, **2013**(04), 016–016 (April 2013).
- [4] J. Suzuki, Y. Inoue, T. Horie, and M. Minowa, Hidden photon cdm search at tokyo, In *"11th Patras Workshop on Axions, WIMPs and WISPs (Axion-WIMP 2015)*. Deutsches Elektronen-Synchrotron, DESY, Hamburg (September 2015).
- [5] N. Tomita, S. Oguri, Y. Inoue, M. Minowa, T. Nagasaki, J. Suzuki, and O. Tajima, *J. Cosmol. Astropart. P.*, **2020**(09), 012–012 (September 2020).
- [6] S. Kotaka et al., *Phys. Rev. Lett.*, **130**(7) (February 2023).
- [7] S. Adachi, R. Fujinaka, Y. Muto, H. Nakata, Y. Sueno, T. Sumida, J. Suzuki, O. Tajima, H. Takeuchi, and S. Honda, *Phys. Rev. D*, **109**(1) (January 2024).
- [8] F. Bajjali et al., *J. Cosmol. Astropart. P.*, **2023**(08), 077 (August 2023).
- [9] S. Knirck et al., *Phys. Rev. Lett.*, **132**(13) (March 2024).
- [10] S. J. Witte, S. Rosauero-Alcaraz, S. D. McDermott, and V. Poulin, *J. High Energy Phys.*, **2020**(6) (June 2020).
- [11] B. Klein, S. Hochgürtel, I. Krämer, A. Bell, K. Meyer, and R. Güsten, *Astron. Astrophys.*, **542**, L3 (May 2012).
- [12] RFSoc (AMD) (Available at: <https://www.amd.com/en/products/adaptive-socs-and-fpgas/soc/zynq-ultrascale-plus-rfsoc.html>, date last accessed January 10, 2025).
- [13] RFSoc 2x2 board (AMD and Hitech Global) (Available at: <https://www.amd.com/en/corporate/university-program/aup-boards/rfsoc2x2.html>, date last accessed January 10, 2025).
- [14] ZeroMQ (Available at: <https://zeromq.org/>, date last accessed January 10, 2025).
- [15] PYNQ (AMD) (Available at: <https://www.pynq.io/>, date last accessed January 10, 2025).
- [16] J.-Y. OH, *IEICE T. Electron.*, **E88-C**(8), 1740–1746 (August 2005).
- [17] M. Garrido, J. Grajal, M. A. Sanchez, and O. Gustafsson, *IEEE Trans. Very Large Scale Integr. (VLSI) Syst.*, **21**(1), 23–32 (January 2013).
- [18] J. W. Cooley and J. W. Tukey, *Math. Comput.*, **19**(90), 297–301 (April 1965).
- [19] G. O’Leary, *IEEE Trans. Audio Electroacoust.*, **18**(2), 177–183 (June 1970).
- [20] H. L. Groginsky and G. A. Works, *IEEE Trans. Comput.*, **C-19**(11), 1015–1019 (November 1970).
- [21] M. Garrido, *J. Signal Process. Sys.*, **94**(11), 1345–1364 (July 2021).
- [22] T. L. Wilson, K. Rohlf, and S. Hüttemeister, *Tools of radio astronomy*, volume 5, (Springer, 2009).
- [23] RFSoc 4x2 board (AMD and RealDigital) (Available at: <https://www.realdigital.org/hardware/rfsoc-4x2>, date last accessed January 10, 2025).